



HAL
open science

A position-dependent acoustic model relevant for some active noise control applications

Chaouki Nacer Eddine Boultifat, Jérôme Lohéac, Mohamed Yagoubi, Philippe Chevrel

► **To cite this version:**

Chaouki Nacer Eddine Boultifat, Jérôme Lohéac, Mohamed Yagoubi, Philippe Chevrel. A position-dependent acoustic model relevant for some active noise control applications. *Journal of Vibration and Control*, 2023, 29 (23-24), pp.5500-5510. 10.1177/10775463221136902 . hal-03619714v2

HAL Id: hal-03619714

<https://hal.science/hal-03619714v2>

Submitted on 17 Oct 2022

HAL is a multi-disciplinary open access archive for the deposit and dissemination of scientific research documents, whether they are published or not. The documents may come from teaching and research institutions in France or abroad, or from public or private research centers.

L'archive ouverte pluridisciplinaire **HAL**, est destinée au dépôt et à la diffusion de documents scientifiques de niveau recherche, publiés ou non, émanant des établissements d'enseignement et de recherche français ou étrangers, des laboratoires publics ou privés.

A position-dependent acoustic model relevant for some active noise control applications

Chaouki N. E. Boultifat¹ Jérôme Lohéac² Mohamed Yagoubi³
Philippe Chevrel³

October 17, 2022

Abstract

This paper focuses on acoustic modeling for active noise control applications. The desired model must be finite dimensional and efficient numerically to meet implementation requirements. It must also be parameterized by the position considered inside the cavity. This additional characteristic is desirable for addressing specific active noise control applications such as optimizing microphone placement, estimating acoustic pressure at different positions of the considered cavity and finally attenuating noise level in a subarea of the cavity.

The main contribution of this paper is to propose a finite-dimensional, low-order, and parameterized acoustic model of a cavity, suitable for active noise control applications. The resulting model is defined as a gray box that combines a one-dimensional analytical model of acoustic propagation, which handles the physical parameterization, and a black-box model that copes with actuator and sensor dynamics as well as modeling errors. The parameters of the proposed model are optimized in order to reproduce the frequency behavior of the real system (LS2N active noise control platform) in a frequency range. This model allows one to accurately reproduce the dynamics at any position in the considered cavity. The prediction performance of the proposed model was compared to a classical black-box model (usually used for active noise control applications) and validated experimentally using the LS2N active noise control platform. The analysis highlighted that the proposed gray-box model can predict the acoustic behavior in a great range of positions. This paper focuses on acoustic modeling for active noise control applications. The desired model must be finite dimensional and efficient numerically to meet implementation requirements. It also must be parameterized by the position considered inside the cavity. This additional characteristic is desirable for addressing specific active noise control applications such as optimizing microphone placement, estimating acoustic pressure at different positions of the considered cavity and finally attenuating noise level in a subarea of the cavity.

keywords: Position-dependent acoustic model, finite-dimensional model, active noise control

1 Introduction

Most control strategies used in active noise control (ANC) applications are based on an acoustic model. Different approaches to derive such model are available, each of them having its own strengths and weaknesses.

Black-box identification methods are probably the most commonly used. They are involved in mono- and multipoint noise attenuation applications, see [23, 2, 3, 25, 14, 26], and in virtual

¹Expleo, 3 avenue des Prés 78180 Montigny-le-Bretonneux, France

²Université de Lorraine, CNRS, CRAN UMR 7039 Nancy, France

³IMT-Atlantique, LS2N UMR CNRS 6004 Nantes, France

microphones designs, see [8, 22, 20, 7]. They generally involve finite dimensional models that are efficient numerically (acceptable model order) with strong prediction performances. One should note, however, that these models are only valid at particular positions in the cavity. The position of the microphone(s) is not an explicit parameter of these models. Consequently, black-box acoustic models do not allow noise attenuation or estimation continuously in a whole volume of a cavity, but only at specific positions.

An alternative to black-box identification is the gray-box approach based on the wave equation. The resulting models involve physical parameters, see [9, 28], and describe acoustic behavior inside the cavity, not only at particular positions. Analytical models obtained from the wave equation are infinite dimensional and generally need to be approximated with finite-dimensional models for use in ANC applications. They can only be derived for systems with simple geometries and boundary conditions. If the analytical approach fails, one can still solve the wave equation numerically using, for instance, finite differences or finite elements methods. However, the resulting models usually involve numerous parameters. For all these reasons, models derived from analytical and numerical solutions of the wave equation are of limited use in ANC applications, [11, 15, 1]. The particularity of the methodology proposed in this paper, when compared to previous works, lies in the fact that it takes advantage of both black and gray-box approaches to provide a cavity acoustic model that is suitable for ANC applications, [24, 31, 16]. That is a finite-dimensional, low-order and parameterized model. The later is defined as a gray box that combines a one-dimensional analytical model of acoustic propagation, which handles the physical parameterization and a black-box model that copes with actuator and sensor dynamics as well as modeling errors. The parameters of the proposed model are optimized in order to reproduce the frequency behavior of the real system (LS2N active noise control platform) in a frequency range, with good prediction performances. In addition to these features, the proposed acoustic model also relies on a physical parameterization (speed of sound, impedances and microphone position) and, in this sens, it is different from the models proposed in other works as for instance in [16]. In this paper, a SEA (Statistical Energy Analysis) model is proposed where the structural and acoustic coupling system is divided into several subsystems, and the power balance equations are used to describe the entire system. Note that such a strategy will not lead to a position dependent model, unlike the approach proposed in the current paper, which is less suitable for addressing issues related to noise attenuation (control) and noise estimation in the entire volume of a cavity.

This model could also be used to optimize microphones positions depending on estimation and control objectives or, alternatively, to estimate online the microphones positions in case they slightly change during operation. These ANC applications can be seen as perspectives of the present paper, which only focuses on the acoustic modelling stage.

The paper is organized as follows: Section 2 presents the ANC platform used for model validation. Section 3 then outlines the proposed methodology, while Section 4 deals with the validation of the methodology and its comparison with the system-identification-based approach. Results and contributions are summarized in the conclusion.

2 Experimental setup: LS2N Box

As mentioned in the introduction, the proposed methodology is applied and validated on an ANC experimental platform. This demonstrator is presented in Figure 1. It consists of a rectangular cavity made of plywood, except for the top, which is composed of acrylic glass. The thickness of the plywood is $2 \cdot 10^{-2}$ m and the one of the acrylic glass is 10^{-2} m. It is instrumented with three speakers and up to five microphones.

Sensors and actuators are connected to the data acquisition card/board through their respective amplifiers. The acquisition card is driven from Simulink through the real-time windows target

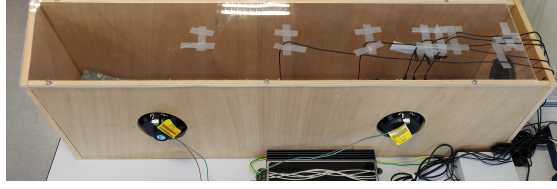


Figure 1: LS2N box.

toolbox of `Matlab`. The sampling frequency used is 10^4 Hz.

In this paper, only one microphone and one speaker are used (as shown in Figure 2) for measuring useful system frequency responses. As depicted in Figure 2, ξ designates the position along the longest axis of the LS2N Box.

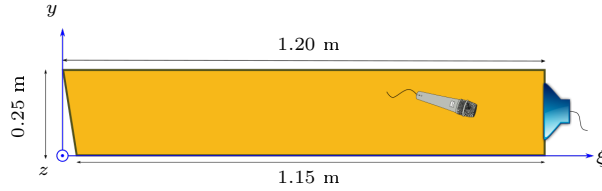


Figure 2: Scheme of the LS2N Box (top view), the height (z axis) measures 0.3 m. The thickness of the plywood is $2 \cdot 10^{-2}$ m and the one of the acrylic glass is 10^{-2} m.

Figure 3 illustrates three typical frequency responses (denoted G_{exp}) of this system (measured in the same y - z plane). The significant number of modes below 1000 Hz makes the demonstrator a relevant test bench for ANC applications. The superposition of the three responses in low frequency indicates that the acoustic field can be considered one-dimensional in low frequency (below 600 Hz). This result was expected because the first cross section modes in y - and z -direction cut on at 680 Hz and 566 Hz, respectively.

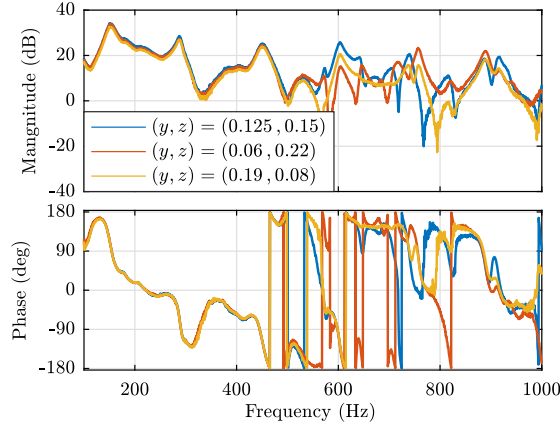


Figure 3: Experimental frequency response G_{exp} at $\xi = 0.8$ m.

3 Model synthesis

The proposed modeling approach is presented in three steps. The model structure is first outlined. Next, the parameters of the proposed model are optimized to fit the experimental response of the system. Finally, the resulting infinite-dimensional model, G_{app}^∞ , is approximated by a finite-dimensional model, G_{app}^N , which is the proposed acoustic model for ANC.

3.1 Structure of the mixed model of infinite order: G_{app}^∞

The objective of the G_{app}^∞ model presented in this section is to reproduce the above-mentioned experimental response. This experimental response is composed of the acoustic response of the system, along with the sensor and actuator dynamics. As Figure 3 demonstrates, the acoustic behavior is mainly one dimensional. This is particularly the case, to a certain extent, with the passenger compartment of a mobile device such as car, trains, airplanes. . . Thus, the proposed structure for G_{app}^∞ is as follows:

$$G_{app}^\infty(s, \xi) = G_{1D}^\infty(s, \xi) G_{extra}(s). \quad (1)$$

In this expression, $G_{1D}^\infty(s, \xi)$ is a one dimensional acoustic model, while $G_{extra}(s)$ is a transfer function (independent of the position) introduced to handle the speaker and microphone dynamics and the potential modeling errors caused by the strong hypothesis made during the construction of G_{1D}^∞ . Both parts of the model are further explained below.

3.1.1 Acoustic part: G_{1D}^∞ .

The analytical model G_{1D}^∞ is based on the following one-dimensional wave equation:

$$\frac{\partial^2 p}{\partial t^2}(t, \xi) = c^2 \frac{\partial^2 p}{\partial \xi^2}(t, \xi) - \frac{1}{Z_l} \frac{\partial p}{\partial t}(t, \xi) \quad (\xi \in (0, L), t > 0), \quad (2)$$

with the following boundary conditions (at $\xi = 0$ and $\xi = L$), see [29, 30, 12, 21]:

$$\frac{\partial p}{\partial \xi}(t, 0) = \frac{1}{Z_0} \frac{\partial p}{\partial t}(t, 0), \quad (t > 0), \quad (3a)$$

$$\frac{\partial p}{\partial \xi}(t, L) = -\frac{1}{Z_1} \frac{\partial p}{\partial t}(t, L) + u(t), \quad (t > 0). \quad (3b)$$

In these expressions, p is the pressure; ξ is the position along the main axis of the cavity; c is the speed of sound; Z_0 is the impedance at position $\xi = 0$; Z_l is the impedance for every $\xi \in (0, L)$; Z_1 is the impedance at position $\xi = L$; and $u(t)$ is the signal applied by the speaker, which is positioned at $\xi = L$. The numerical value L equals 1.175 m.

Remark 1. *In the rest of this paper, we assume that the acoustic impedances Z_0 , Z_1 and Z_l are constant and independent of the frequency of excitation. We also recall that acoustic impedances are usually complex numbers. Their imaginary parts reflect the flexibility of the boundary, while their real part reflect the damping, see e.g. [21, § 6.6]. This assumption leads to the fact that the these impedances are real. In addition, since acrylic glass is more reflective than wood, it is also expected that Z_l is larger than Z_0 and Z_1 . All these facts will be confirmed in Table 1, where we give values of these parameters, see also Remark 4.*

The resulting analytical transfer function G_{1D}^∞ from u to p is derived by applying the Laplace transform in time to (2) and (3) (initial conditions are assumed to be zero). This approach leads to the following equations where \bar{p} and \bar{u} denote the Laplace transforms of p and u , respectively, and where s is the Laplace variable:

$$\left(s^2 + \frac{s}{Z_l}\right) \bar{p}(s, \xi) = c^2 \frac{\partial \bar{p}}{\partial \xi^2}(s, \xi) \quad (\xi \in (0, L)), \quad (4)$$

$$\frac{\partial \bar{p}(s, 0)}{\partial \xi} = \frac{s}{Z_0} \bar{p}(s, 0), \quad (5a)$$

$$\frac{\partial \bar{p}(s, L)}{\partial \xi} = -\frac{s}{Z_1} \bar{p}(s, L) + \bar{u}(s). \quad (5b)$$

The general solution of (4) is of the form:

$$\bar{p}(s, \xi) = \mathcal{A}(s) \sinh(\kappa(s)\xi) + \mathcal{B}(s) \cosh(\kappa(s)\xi). \quad (6)$$

In this expression, $\kappa(s)$ is defined as follows:

$$\kappa(s) = \frac{1}{c} \sqrt{s^2 + \frac{s}{Z_l}}. \quad (7)$$

While the coefficients $\mathcal{A}(s)$ and $\mathcal{B}(s)$ are obtained when applying boundary constraints (5a) and (5b):

$$\mathcal{A}(s) = \frac{\bar{u}(s)}{\mathcal{D}(s)}, \quad \mathcal{B}(s) = \frac{Z_0 \kappa(s)}{s} \frac{\bar{u}(s)}{\mathcal{D}(s)},$$

with

$$\mathcal{D}(s) = \left(\kappa(s) + \frac{Z_0 \kappa(s)}{Z_1}\right) \cosh(\kappa(s)L) + \left(\frac{s}{Z_1} + \frac{Z_0 \kappa^2(s)}{s}\right) \sinh(\kappa(s)L).$$

It finally leads to the following transfer function:

$$G_{1D}^\infty(s, \xi) = \frac{\bar{p}(s, \xi)}{\bar{u}(s)} = \frac{\sinh(\kappa(s)\xi) + \frac{Z_0 \kappa(s)}{s} \cosh(\kappa(s)\xi)}{\mathcal{D}(s)}. \quad (8)$$

This transfer function reproduces only the acoustic behavior. It is parameterized with three impedances (Z_0 , Z_1 and Z_l), the speed of sound c , and the length of the cavity L (whose values are taken from Table 1).

Remark 2. *One can easily confirm that the relation (8) is independent of the choice of the complex root determination made in (7). Indeed, let us set $(s^2 + s/Z_l)/c^2 = \rho e^{i\theta}$, with $\rho \in \mathbb{R}_+$ and $\theta \in \mathbb{R}$. It is well-known that $\sqrt{\rho e^{i\theta}} = \exp(\ln(\rho e^{i\theta})/2)$, but, the \ln function is not defined on the whole complex plane. However, whatever the choice of determination is, we have $\ln e^{i\theta} \in \{i(\theta + 2k\pi) \mid k \in \mathbb{Z}\}$. Hence, we have, $\sqrt{\rho e^{i\theta}} \in \{-\sqrt{\rho} e^{i\theta/2}, \sqrt{\rho} e^{i\theta/2}\}$. Injecting these two possibilities in (8), leads to the same expression, i.e., G_{1D}^∞ is independent of the root determination used to define κ .*

3.1.2 Extra part: G_{extra} .

As mentioned previously the extra part of the model G_{extra} represents the speaker and microphone dynamics and the potential model errors. In this paper, its order is set to 10 (i.e., slightly higher than typical speaker and microphone models, both of which are order 3 and only valid in low frequency, see [13]). This order can be adjusted if necessary (e.g., according to the frequency range considered).

3.2 Model parameters optimization

Once the structure of the model is defined, all the model's parameters (Z_0 , Z_1 , Z_l , c , L , and the numerator and denominator coefficients of G_{extra}) are optimized to fit the experimental frequency response of the system G_{exp} . The optimized criterion J is given by:

$$J = \frac{\|G_{exp}(\cdot, \xi_r) - G_{app}^\infty(\cdot, \xi_r)\|_{2, [\omega_-, \omega_+]}}{\|G_{exp}(\cdot, \xi_r) - E_{\omega_-}^{\omega_+}(G_{exp}(\cdot, \xi_r))\|_{2, [\omega_-, \omega_+]}}. \quad (9)$$

In this expression, ω_- and ω_+ are respectively the lower and upper pulsations of the considered frequency range. In addition, the average $E_{\omega_-}^{\omega_+}$ and the norm $\|\cdot\|_{2, [\omega_-, \omega_+]}$ are respectively defined by

$$E_{\omega_-}^{\omega_+}(f) = \int_{\omega_-}^{\omega_+} f(j\omega) d\omega \quad \text{and} \quad \|f\|_{2, [\omega_-, \omega_+]}^2 = \int_{\omega_-}^{\omega_+} |f(j\omega)|^2 d\omega. \quad (10)$$

Remark 3. Only discretized expressions of the average $E_{\omega_-}^{\omega_+}$ and the norm $\|\cdot\|_{2, [\omega_-, \omega_+]}$ given by (10) will be used in the sequel.

The optimization of G_{app}^∞ is carried out using the experimental frequency response G_{exp} (presented in Figure 3 [blue line, $y = 0.125$ and $z = 0.15$]) obtained at a single reference position $\xi_r = 0.8$ m and over the frequency range $\omega \in [\omega_-, \omega_+] = [100, 1000]$ Hz. The frequency step, used for the discretization (see Remark 3), is 0.3 Hz.

Several gradient-based and meta-heuristic optimization methods were tested unsuccessfully. This is due either to an unsatisfactory performance or a high number of decision variables. The well-known Particle Swarm Optimization (PSO) meta-heuristic (see [10, 28]) seems, however, to yield satisfactory results. The values of the parameters of G_{app}^∞ after PSO optimization are given in Table 1.

Table 1: Model-optimized parameters values.

Parameter	Value
Z_l	6.70×10^{12} m/s
Z_0	8.00×10^6 m/s
Z_1	1.08×10^3 m/s
c	3.48×10^2 m/s
L	1.175 m

Remark 4. For the particle swarm optimization, we also optimize c and L . Indeed, the sound celerity depends on external physical parameters (such as temperature and humidity), and in the algorithm, we allow c to range in $[330, 350]$ m/s. Similarly, since the considered cavity does not have a cuboid shape, we let L range in $[1.15, 1.2]$ m (these two bounds are the minimal and maximal length of the considered cavity).

In addition, as mentioned in Remark 1, the impedances are complex numbers. We did the optimization with complex impedances, and get a tiny imaginary part (of order 10^{-1}). We hence decide to neglect it. This is in accordance with the fact that the boundaries of the cavity are rigid. In addition, as expected in Remark 1, we observe that $Z_l > \max\{Z_0, Z_1\}$, and latter, we will consider that $Z_l = \infty$, that is to say that the acrylic glass boundary is perfectly reflective (see e.g. [30, § III.B]).

Remark 5. The unit of Z_l , Z_0 and Z_1 does not correspond to that of an impedance. In fact, Z_l (and similarly Z_0 and Z_1) is of the form $Z_l = Z'_l/\rho$, where ρ is the air density, and Z'_l is an impedance whose unit is $\text{kg.m}^{-2}.\text{s}^{-1}$.

3.3 Reduced-order model: G_{app}^N

The optimization of the model parameters was conducted on infinite-dimensional model G_{app}^∞ . It is now necessary to approximate this model by a finite-dimensional model denoted G_{app}^N . The infinite-dimensional component of G_{app}^∞ is G_{1D}^∞ (G_{extra} is already finite dimensional). Thus, approximating G_{app}^∞ is equivalent to reducing G_{1D}^∞ to the finite-dimensional model denoted G_{1D}^N . Model G_{app}^N is consequently defined as follows:

$$G_{app}^N(s, \xi) = G_{1D}^N(s, \xi) G_{extra}(s). \quad (11)$$

Beforehand, an additional hypothesis is introduced regarding impedance Z_l . Its value, very high in Table 1, may be set to infinity without causing significant deterioration of the model frequency response. With this assumption, $\kappa(s)$ becomes $\kappa(s) = s/c$ and G_{1D}^∞ can be rewritten as follows:

$$G_{1D}^\infty(s, \xi) = \frac{1}{s} \frac{Z_0 Z_1}{Z_0 + Z_1} \frac{\frac{c}{Z_0} \sinh \frac{s\xi}{c} + \cosh \frac{s\xi}{c}}{\frac{c^2 + Z_0 Z_1}{c(Z_0 + Z_1)} \sinh \frac{sL}{c} + \cosh \frac{sL}{c}}. \quad (12)$$

The approach used to approximate this model is based on Cauchy residues. First, the infinite partial-fraction expansion (see [5]) of $s \times G_{1D}^\infty$ is derived. This infinite sum is then truncated to obtain a finite dimensional model. The truncation order is chosen to ensure an acceptable level of *fit* between the frequency response of $s \times G_{1D}^\infty$ and its finite dimensional approximation $s \times G_{1D}^N$.

3.3.1 Infinite partial-fraction expansion of $s \times G_{1D}^\infty$.

Deriving the infinite partial-fraction expansion of $s \times G_{1D}^\infty(s, \xi)$ requires the explicit expression of its poles p_k :

$$p_k = p_0 + j \frac{c\pi k}{L} \quad (k \in \mathbb{Z}), \quad \text{with} \quad (13a)$$

$$p_0 = \frac{c}{2L} \ln \left(\frac{c^2 + Z_0 Z_1 - c(Z_0 + Z_1)}{c^2 + Z_0 Z_1 + c(Z_0 + Z_1)} \right). \quad (13b)$$

The above expressions are valid for $Z_0 > c$ and $Z_1 > c$, conditions which are satisfied here (see Table 1). Furthermore, all the poles of $s \times G_{1D}^\infty$ are simple, p_k is the complex conjugate of p_{-k} , and in particular, p_0 is real.

Using trigonometric relations, $s \times G_{1D}^\infty(s, \xi)$ can be expressed as

$$s \times G_{1D}^\infty(s, \xi) = C \left(A(\xi) \frac{\sinh \frac{\xi(s - p_0)}{c}}{\sinh \frac{L(s - p_0)}{c}} + B(\xi) \frac{\cosh \frac{\xi(s - p_0)}{c}}{\sinh \frac{L(s - p_0)}{c}} \right), \quad (14)$$

with

$$C = \frac{Z_0 Z_1}{Z_0 + Z_1} \frac{1}{\frac{c^2 + Z_0 Z_1}{c(Z_0 + Z_1)} \cosh \frac{p_0 L}{c} + \sinh \frac{p_0 L}{c}},$$

$$A(\xi) = \frac{c}{Z_0} \cosh \frac{\xi p_0}{c} + \sinh \frac{\xi p_0}{c} \quad \text{and}$$

$$B(\xi) = \frac{c}{Z_0} \sinh \frac{\xi p_0}{c} + \cosh \frac{\xi p_0}{c}.$$

Based on the above expression and on the infinite partial-fraction expansion given in [5] (see also [6, Section 4.3 and Exercise 4.24]), the transfer function $s \times G_{1D}^\infty$ given by (12) is rewritten as follows, for every $\xi \in [0, L)$:

$$s \times G_{1D}^\infty(s, \xi) = \frac{a_0(\xi)}{s - p_0} + \sum_{k=1}^{+\infty} \left(\frac{a_k(\xi)}{s - p_k} + \frac{a_{-k}(\xi)}{s - p_{-k}} \right), \quad (15)$$

where the coefficients $a_k(\xi)$ are the residues of $s \times G_{1D}^\infty$ in p_k ,

$$a_k(\xi) = \text{res}(s \times G_{1D}^\infty, p_k) = \lim_{s \rightarrow p_k} (s - p_k) s \times G_{1D}^\infty(s, \xi) = \frac{f(p_k, \xi)}{g'(p_k)},$$

where f and g are respectively the numerator and denominator of $s \times G_{1D}^\infty$ (recall that all the poles of $s \times G_{1D}^\infty$ are simple). It is easy to check that $a_{-k}(\xi)$ is the complex conjugate of $a_k(\xi)$ and, in particular, that $a_0(\xi)$ is a real number. Consequently, $s \times G_{1D}^\infty$, given by (15), can be expressed as

$$s \times G_{1D}^\infty(s, \xi) = \frac{a_0(\xi)}{s - p_0} + 2 \sum_{k=1}^{\infty} \frac{s \Re(a_k(\xi)) - \Re(p_k a_{-k}(\xi))}{s^2 - 2\Re(p_k)s + |p_k|^2}, \quad (16)$$

where $\Re(\cdot)$ is the real part of a complex number.

Remark 6. *An analytical validation of expression (16) is provided in Appendix A, which explains in particular why the relation is not valid for $\xi = L$.*

3.3.2 Reduced-order transfer function $s \times G_{1D}^N$.

The transfer function $s \times G_{1D}^N(s, \xi)$ of reduced order is designed to approximate the behavior of the system (12) on a predefined range of frequencies. To construct this transfer function, expression (16) is truncated up to a large enough order $N \geq 1$. The following reduced-order transfer function is considered:

$$s \times G_{1D}^N(s, \xi) = \frac{a_0(\xi)}{s - p_0} + 2 \sum_{k=1}^N \frac{s \Re(a_k(\xi)) - \Re(p_k a_{-k}(\xi))}{s^2 - 2\Re(p_k)s + |p_k|^2}. \quad (17)$$

The integer N is large enough so that the transfer function of reduced order matches the system (12) in a predefined frequency range and for every $\xi \in [0, \Xi]$ (with $\Xi \in (0, L)$ given *a priori*).

3.3.3 Numerical validation of the finite order model.

The value of N is set to $N = 20$. Model G_{1D}^N is consequently of order $2(N + 1) = 42$. Figure 4 compares the frequency responses of G_{1D}^∞ and G_{1D}^N for $\xi = 0.8$ m.

The indicator used to evaluate the accuracy of the approximated model is denoted *fit*. This indicator quantifies how the frequency response of a given model \widehat{G} matches the reference frequency response G_{ref} , and is defined by

$$fit = 100 \left(1 - \frac{\|G_{ref} - \widehat{G}\|_{2, [\omega_-, \omega_+]}}{\|G_{ref} - \mathbf{E}_{\omega_-}^{\omega_+}(G_{ref})\|_{2, [\omega_-, \omega_+]}} \right)^+. \quad (18)$$

The notations in (18) are the same as in (10), and f^+ is the positive part of f . A *fit* value of 100 would mean a perfect match between the given model and the reference (in terms of frequency response). The *fit* indicator is indeed the R^2 -indicator, see [4] and references therein. Let us also mentioned that this indicator has also been used previously, for instance in [17, 18].

Figure 5 presents the *fit* indicator (defined by (18) with $G_{ref} = G_{1D}^\infty$, $\hat{G} = G_{1D}^N$, $\omega_- = 10^2$ Hz and $\omega_+ = 10^3$ Hz, the frequency step used for the discretization, see Remark 3, is of $5 \cdot 10^{-2}$ Hz) obtained with respect to the position ξ . As in [1], a very close match between the finite- and infinite-dimensional models is obtained. The degradation visible in Figure 5 for ξ values close to L is due, as expected, to the fact that equation (17) is not valid for $\xi = L$ (see Remark 6).

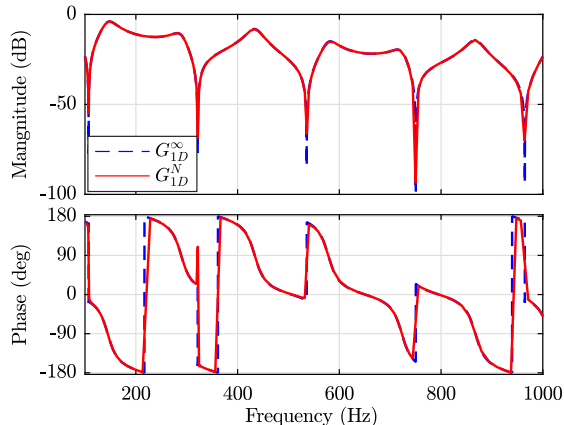


Figure 4: Frequency response of G_{1D}^∞ and G_{1D}^N at $\xi = 0.8$ m ($y = 0.125$ m, $z = 0.15$ m).

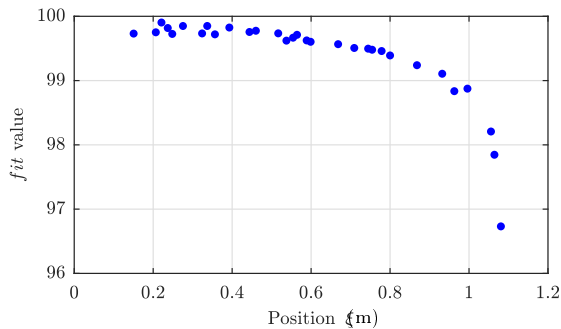


Figure 5: Fit indicator value between G_{1D}^∞ and G_{1D}^N according to ξ .

4 Experimental validation

To evaluate the performance of the proposed model, in this section, we compare it to the system identification approach. Thus, the black-box model is presented first and then compared to the proposed approach.

4.1 Black-box model: G_{bb}

This section deals with obtaining a black-box model able to reproduce the experimental response presented in Figure 3 (blue line) through identification. Different identification algorithms can be used for ANC applications. As detailed in [19], ANC designers mainly use time approaches. In this paper, the identification should allow to match the frequency response of the reference model. The selected method is consequently based on a frequency approach and makes use of the subspace N4SID algorithm, see [27]. This algorithm is non-iterative. It only requires the *a priori* model order and gives a full state space realization as a result. This algorithm has proven its efficiency for previous ANC applications involving the LS2N Box, see [17, 19]. A possible alternative to the subspace method is using a prediction-error method that optimizes *e.g.* a model in a companion form. Although the number of decision variables is reduced, using the canonical companion state-space form, it is still high, and results of the prediction error method are not always satisfying. This problem is due to poor conditioning of the canonical form for high-order models, and the increased risk of getting local optima. The latter risk may be avoided by initializing the prediction error method with the result of the subspace method. However, the result, when acceptable, is not significantly improved, indicating that the subspace method result is near optimal.

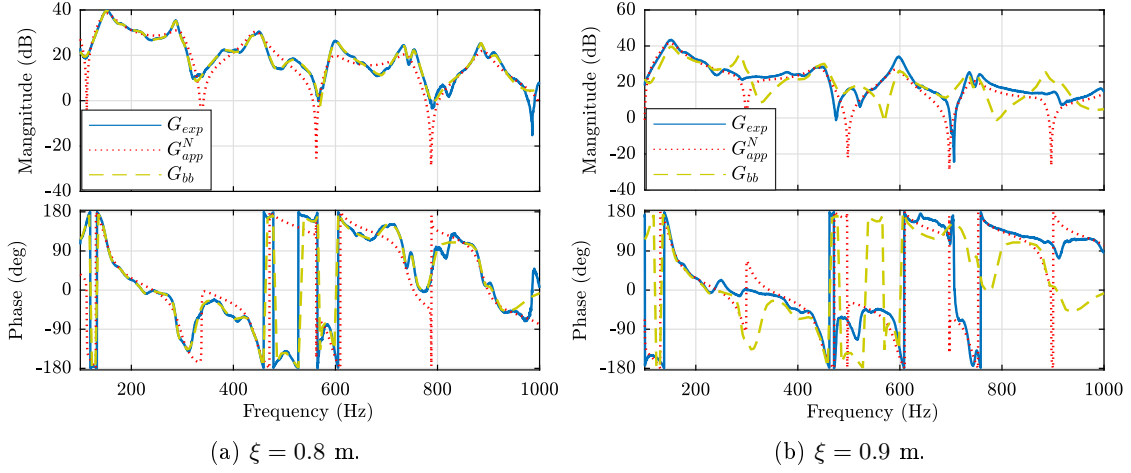
The identification is conducted at the single reference position $\xi = 0.8$ m previously used to optimize the parameters of G_{app}^∞ . The order of the identified model is 52, and its frequency validity range is [100-1000] Hz.

4.2 Parameterized gray-box and black-box models compared

Both the G_{app}^N and G_{bb} models were identified using the experimental frequency response obtained at position $\xi = 0.8$ m. The comparison between the two models and the experimental data at this position is given in Figure 6a. Each model was also compared to the experimental data obtained at different positions: $\xi = 0.9$ m in Figure 6b and $\xi = 0.4$ m in Figure 6c. Given that G_{app}^N is parameterized with the position while G_{bb} is not, only the former is able to predict the acoustic pressure at points relatively far from the microphone used for the identification stage. At each position ξ where experimental data were measured, a *fit* value was calculated for each model. The resulting evolution of the *fit* indicator according to the position ξ is given in Figure 7. This *fit* is the one given in (18) with $G_{ref} = G_{exp}$ and $\hat{G} = G_{app}^N$ or $\hat{G} = G_{bb}$, $[\omega_-, \omega_+] = [100, 1000]$ Hz. The frequency step, used for the discretization, is 5.10^{-2} Hz.

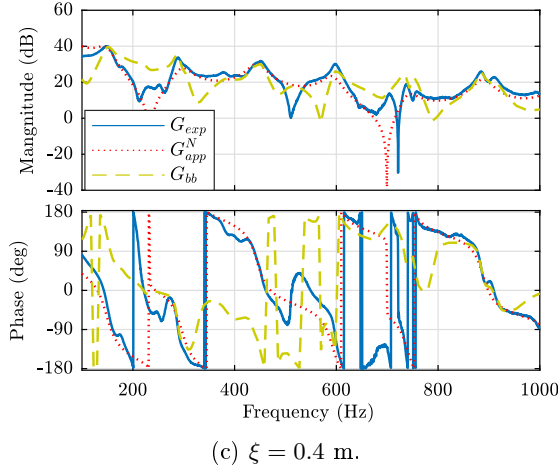
At the reference position $\xi = 0.8$ m, G_{bb} performs better than G_{app}^N . However, it is worse than G_{app}^N at positions $\xi = 0.9$ m and $\xi = 0.4$ m. These results are illustrated in Figure 7, which highlights that the identified model G_{bb} performs better than G_{app}^N around the reference position, but rapidly (from 5.10^{-2} m) weakens when moving away from this position. The *fit* values obtained with G_{app}^N also decrease when moving away from the reference position but remain acceptable, as seen in Figure 6c, which compares the experimental frequency response with the proposed model response at the position where the worst fit value was obtained. This expected result can be summarized as follows: The identified model G_{bb} is more accurate than the proposed model G_{app}^N at a precise position (especially for more complex geometries and boundary conditions), but fails to accurately reproduce the acoustic behavior in the cavity on a large spatial range because the position dependence is not mastered.

One may also note the anti-resonances of the model G_{app}^N , which are not present in the experimental response of the system. This difference does not seem significant in broadband applications because it only affects the frequencies where the gain of the system is relatively low. Optimized impedances that are purely real (see Remarks 1 and 4) can also relate to the anti-resonance frequency mismatch as noted in the experimental validation. In future works we will try to improve this part by adding new optimization parameters.



(a) $\xi = 0.8$ m.

(b) $\xi = 0.9$ m.



(c) $\xi = 0.4$ m.

Figure 6: Experimental frequency responses ($y = 0.125$ m, $z = 0.15$ m).

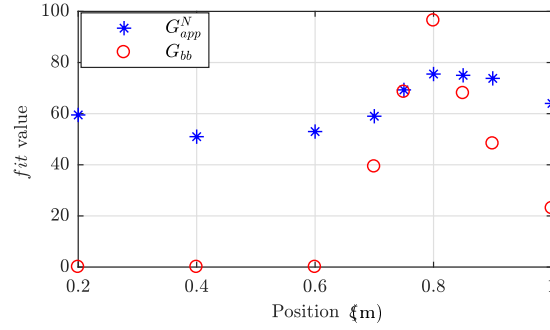


Figure 7: Evolution of the *fit* indicator according to ξ .

After having compared the performances of the models, one may also be interested in comparison between the characteristics of the two models. This comparison is provided in Table 2. Although they are of similar order, the number of decision variables is completely different for G_{app}^N

and G_{bb} . Whereas G_{bb} has a full state-space representation of order fifty-two and all its parameters are manipulated by the subspace algorithm, G_{app}^N has only five physical parameters (three impedances, the speed of sound, and the length of the cavity) plus nineteen parameters from the numerator and denominator of G_{extra} to be optimized. Thus, the proposed model is parsimonious in terms of decision variables. Furthermore, G_{extra} being a low-order transfer function, it does not introduce conditioning problems. Finally, whereas G_{app}^N masters the position dependence, G_{bb} does not.

Table 2: Experimentation models characteristics.

	G_{app}^N	G_{bb}
Order	52	52
Number of decision variables	(5+19=) 24	2808
Parameters with physical meaning	Partially	No
Explicit position dependence	Yes	No

Remark 7. *As already mentioned, using a prediction error approach and a model in the companion form for G_{bb} would reduce the number of decision variables, but would also introduce conditioning and optimization problems.*

Let us mention that increasing the number of decision variables in the black-box model, might not help to have a better fit outside the reference position. Indeed, for this task, one shall do more measurements and perform an identification at all measurement points. While for the proposed model, the fit can be increased by increasing N , this, up to some limit, which relies on how the one-dimensional wave equation well represent the wave equation set in the acoustic cavity. For complex geometries, obtaining G_{app}^N is not so easy, and relies on the computation of the eigenvalues of the Laplace operator. In the present paper, the elongated geometry of the LS2N cavity allows us to reduce our self to the one-dimensional wave equation, and G_{1D}^N can be explicitly computed. Finally, let us also mention that obtaining G_{app}^N requires more analytical work than obtaining G_{bb} .

5 Conclusion

The main contribution of this paper is that it proposes a finite-dimensional, low-order, and parameterized acoustic model of a cavity suitable for ANC applications. The resulting gray-box model allows one to accurately reproduce the dynamics at any position in the considered cavity. It is based on a basic one-dimensional acoustic propagation model and on a low-order transfer function that handles the actuator and sensor dynamics and the remaining model errors (mainly due to the one-dimensional assumption). The prediction performance of the proposed model was compared to a classical black-box model. The analysis highlighted that the proposed gray-box model can predict the acoustic behavior in a great range of positions, while the black-box model cannot. The reason is that the gray-box model is parameterized by the position inside the cavity, while the black-box model is not. Finally, the strength of the proposed model resides in its numerical efficiency and its analytic dependency on the position inside the cavity.

It is suitable either to estimate the pressure signal with a single or restricted number of microphones at any position in the cavity or to design a controller aimed at attenuating the noise level in a whole subarea of the cavity.

We can also deal with the problem of modeling obstacles within the study system, to be closer to practical cases. As mentioned at the end of Section 4, obtaining G_{app}^N for complex geometries

might be a challenge. However, we think that for geometries close enough to cuboids, the methodology used in this paper could still be applied, provided that the one-dimensional wave equation is replaced by the three-dimensional one set in a cuboid.

Acknowledgements The authors thank Paul Loiseau for helpful discussions and comments. This work has been initiated while the first and second authors were members of LS2N, and they thank LS2N for hosting and support. The second author is supported by the French ANR projects NICETWEET and TRECOS, grants: ANR-20-CE48-0009 and ANR-20-CE40-0009.

References

- [1] C. Boultifat, P. Chevrel, J. Lohéac, and M. Yagoubi. A parametrized reduced order model of 1D acoustic propagation system for robust spatial multi-point active noise attenuation. In *2018 IEEE Conference on Decision and Control (CDC)*, pages 2968–2975, Miami Beach, FL, United States, Dec. 2018.
- [2] J. C. Carmona and V. M. Alvarado. Active Noise Control of a Duct Using Robust Control Theory. *IEEE Transactions on Control Systems Technology*, 8(6):930–938, 2000.
- [3] J. Cheer. *Active Control of the Acoustic Environment in an Automobile Cabin*. PhD thesis, University of Southampton, Southampton, 2012.
- [4] D. Chicco, M. J. Warrens, and G. Jurman. The coefficient of determination R-squared is more informative than SMAPE, MAE, MAPE, MSE and RMSE in regression analysis evaluation. *PeerJ Computer Science*, 7:e623, 2021.
- [5] R. Curtain and K. Morris. Transfer functions of distributed parameter systems: A tutorial. *Automatica*, 45(5):1101–1116, 2009.
- [6] R. F. Curtain and H. Zwart. *An introduction to infinite-dimensional linear systems theory*, volume 21 of *Texts in Applied Mathematics*. Springer-Verlag, New York, 1995.
- [7] D. P. Das, D. J. Moreau, and B. S. Cazzolato. A computationally efficient frequency-domain filtered-x lms algorithm for virtual microphone. *Mechanical Systems and Signal Processing*, 37(1-2):440–454, 2013.
- [8] J. Diaz, J. Egaña, and J. Viñolas. A local active noise control system based on a virtual-microphone technique for railway sleeping vehicle applications. *Mechanical systems and signal processing*, 20(8):2259–2276, 2006.
- [9] J.-F. Durand, C. Soize, and L. Gagliardini. Structural-acoustic modeling of automotive vehicles in presence of uncertainties and experimental identification and validation. *The Journal of the Acoustical Society of America*, 124(3):1513–1525, 2008.
- [10] R. Eberhart and J. Kennedy. A new optimizer using particle swarm theory. In *MHS’95. Proceedings of the Sixth International Symposium on Micro Machine and Human Science*, pages 39–43, Oct 1995.
- [11] B. Fang, A. Kelkar, S. Joshi, and H. Pota. Modelling, system identification, and control of acoustic-structure dynamics in 3-D enclosures. *Control Engineering Practice*, 12(8):989–1004, 2004.

- [12] A. Hull and C. Radcliffe. Experimental verification of the nonself-adjoint state space duct model. *Journal of Vibration and Acoustics*, 114(3):404–408, 07 1992.
- [13] B. J. Zimmer, S. P. Lipshitz, K. Morris, J. Vanderkooy, and E. E. Obasi. An improved acoustic model for active noise control in a duct. *Journal of Dynamic Systems, Measurement, and Control*, 125(3):382–395, 09 2003.
- [14] I. D. Landau, R. Meléndez, L. Dugard, and G. Buche. Robust and adaptive feedback noise attenuation in ducts. *IEEE Transactions on Control Systems Technology*, 27(2):872–879, March 2019.
- [15] Y. Li, X. Wang, R. Huang, and Z. Qiu. Active vibration and noise control of vibro-acoustic system by using pid controller. *Journal of Sound and Vibration*, 348:57–70, 2015.
- [16] Z. Liu, M. Fard, and J. L. Davy. Prediction of the acoustic effect of an interior trim porous material inside a rigid-walled car air cavity model. *Applied Acoustics*, 165:107325, 2020.
- [17] P. Loiseau, P. Chevrel, M. Yagoubi, and J.-M. Duffal. Investigating achievable performances for robust broadband active noise control in an enclosure. *IEEE Transactions on Control Systems Technology*, 27(1):426–433, Nov. 2017.
- [18] P. Loiseau, P. Chevrel, M. Yagoubi, and J.-M. Duffal. A robust feedback control design for broadband noise attenuation in a car cabin. In *20th IFAC World Congress*, pages 2768–2775, Toulouse, France, 2017.
- [19] P. Loiseau, P. Chevrel, M. Yagoubi, and J.-M. Duffal. Robust active noise control in a car cabin: Evaluation of achievable performances with a feedback control scheme. *Control Engineering Practice*, 81:172–182, 2018.
- [20] D. Moreau, B. Cazzolato, A. Zander, and C. Petersen. A review of virtual sensing algorithms for active noise control. *Algorithms*, 1(2):69–99, 2008.
- [21] D. Nefske and S. Sung. *Noise and Vibration Control Engineering: Principles and Applications, 2nd Edition*. Wiley Online Library, 2005.
- [22] C. D. Petersen, R. Fraanje, B. S. Cazzolato, A. C. Zander, and C. H. Hansen. A kalman filter approach to virtual sensing for active noise control. *Mechanical Systems and Signal Processing*, 22(2):490–508, 2008.
- [23] B. Rafaely and S. J. Elliott. H_2/H_∞ ; active control of sound in a headrest: design and implementation. *IEEE Transactions on Control Systems Technology*, 7(1):79–84, Jan 1999.
- [24] M. A. Sanderson and T. Onsay. Cae interior cavity model validation using acoustic modal analysis. *SAE technical paper*, pages 01–2167, 2007.
- [25] R. Schirmacher, R. Kunkel, and M. Burghardt. Active Noise Control for the 4.0 TFSI with Cylinder on Demand Technology in Audi’s S-Series. In *7th International Styrian Noise, Vibration & Harshness Congress: The European Automotive Noise Conference*. SAE International, jun 2012.
- [26] C. K. Song, J. K. Hwang, J. M. Lee, and J. K. Hedrick. Active vibration control for structural-acoustic coupling system of a 3-d vehicle cabin model. *Journal of Sound and Vibration*, 267(4):851–865, 2003.

- [27] P. Van Overschee and B. De Moor. Continuous-time frequency domain subspace system identification. *Signal Processing*, 52(2):179–194, 1996.
- [28] X. Xu and P. Lin. Parameter identification of sound absorption model of porous materials based on modified particle swarm optimization algorithm. *PLOS ONE*, 16:1–16, 05 2021.
- [29] Z. Yang. Design of active noise control using feedback control techniques for an acoustic duct system. In *IEEE Conference on Robotics, Automation and Mechatronics, 2004.*, volume 1, pages 467–472. IEEE, 2004.
- [30] Z. Yang and S. Podlech. Theoretical modeling issue in active noise control for a one-dimensional acoustic duct system. In *2008 IEEE International Conference on Robotics and Biomimetics*, pages 1249–1254. IEEE, 2009.
- [31] Z. Zhang, Y. Zhang, C. Huang, and X. Liu. Low-noise structure optimization of a heavy commercial vehicle cab based on approximation model. *Journal of Low Frequency Noise, Vibration and Active Control*, 37(4):987–1002, 2018.

A Infinite partial-fraction expansion of $s \times G_{1D}^\infty(s, \zeta)$

In order to obtain the expression (16) from (14), it is enough to show this results for the meromorphic functions $f_\zeta(z) = \frac{\sinh(\zeta z)}{\sinh z}$ and $g_\zeta(z) = \frac{\cosh(\zeta z)}{\sinh z}$, with $\zeta \in [0, 1]$. In fact, this follows from the changes of variables $z = L(s - p_0)/c$ and $\zeta = \xi/L$, and the linearity of the residues.

More precisely, noticing that the set of zeros of \sinh is $j\pi\mathbb{Z}$, and noticing that

$$\begin{aligned} \operatorname{res}(f_\zeta, jk\pi) &= (-1)^k j \sin(k\pi\zeta) \quad \text{and} \\ \operatorname{res}(g_\zeta, jk\pi) &= (-1)^k \cos(k\pi\zeta), \end{aligned}$$

for every $k \in \mathbb{Z}$, our aim is to prove the following lemma.

Lemma A.1. *For every $z \in \mathbb{C} \setminus j\pi\mathbb{Z}$, we have*

$$g_\zeta(z) = \frac{1}{z} + 2z \sum_{k=1}^{\infty} \frac{(-1)^k \cos(k\pi\zeta)}{z^2 + (k\pi)^2} \quad (\zeta \in [0, 1]) \quad (19)$$

and

$$f_\zeta(z) = 2 \sum_{k=1}^{\infty} \frac{(-1)^{k+1} k\pi \sin(k\pi\zeta)}{z^2 + (k\pi)^2} \quad (\zeta \in [0, 1]). \quad (20)$$

The proof of (19) is classical and similar to the infinite partial fraction expansions given in [5] (see also [6, Section 4.3]), and is given here for the sake of completeness. We however think that the proof of (20) is more tricky, and we did not find similar computation in the literature.

Proof. Let us first prove the equality (19).

Let us first note that for every given $z \in \mathbb{C} \setminus j\pi\mathbb{Z}$ and every $k \in \mathbb{Z}$, we have

$$\operatorname{res}\left(\frac{g_\zeta(\cdot)}{z - \cdot}, jk\pi\right) = \frac{(-1)^k \cos(k\pi\zeta)}{z - jk\pi} \quad \text{and} \quad \operatorname{res}\left(\frac{g_\zeta(\cdot)}{z - \cdot}, z\right) = -g_\zeta(z).$$

Let $(a_n)_{n \in \mathbb{N}^*}$ and $(b_n)_{n \in \mathbb{N}^*}$ be two sequences of real positive numbers, such that $b_n \notin \pi\mathbb{Z}$ and $\lim_{n \rightarrow \infty} a_n = \lim_{n \rightarrow \infty} b_n = \infty$. We define

$$D_n = \{x + jy \mid (x, y) \in [-a_n, a_n] \times [-b_n, b_n]\}.$$

Given $z \in \mathbb{C} \setminus j\pi\mathbb{Z}$, for $n \in \mathbb{N}$ large enough (n shall be such that $z \in D_n$), the Cauchy residue Theorem ensures that

$$\begin{aligned} \frac{1}{2j\pi} \oint_{\partial D_n} \frac{g_\zeta(s)}{z-s} ds &= -g_\zeta(z) + \sum_{\substack{k \in \mathbb{Z} \\ |k\pi| < b_n}} \frac{(-1)^k \cos(k\pi\zeta)}{z - jk\pi} \\ &= -g_\zeta(z) + \frac{1}{z} + 2 \sum_{\substack{k \in \mathbb{N}^* \\ k\pi < b_n}} \frac{(-1)^k \cos(k\pi\zeta)}{z^2 + (k\pi)^2}. \end{aligned}$$

Consequently, in order to prove the result, it is enough to show that

$$\lim_{n \rightarrow \infty} \oint_{\partial D_n} \frac{g_\zeta(s)}{z-s} ds = 0,$$

for a particular choice of sequences $(a_n)_n$ and $(b_n)_n$. For every $n \in \mathbb{N}^*$, we define,

$$\begin{aligned} X_n &= \int_{-a_n}^{a_n} \frac{g_\zeta(x - jb_n)}{z - x + jb_n} dx + \int_{a_n}^{-a_n} \frac{g_\zeta(x + jb_n)}{z - x - jb_n} dx, \\ Y_n &= \int_{-b_n}^{b_n} \frac{g_\zeta(a_n + jy)}{z - a_n - jy} dy + \int_{b_n}^{-b_n} \frac{g_\zeta(-a_n + jy)}{z + a_n - jy} dy, \end{aligned}$$

so that $\oint_{\partial D_n} \frac{g_\zeta(s)}{z-s} ds = X_n + jY_n$.

Noticing that $g_\zeta(-z) = -g_\zeta(z)$, we easily obtain that

$$\begin{aligned} X_n &= 2z \int_{-a_n}^{a_n} \frac{g_\zeta(x - jb_n)}{z^2 - (x - jb_n)^2} dx, \\ Y_n &= 2z \int_{-b_n}^{b_n} \frac{g_\zeta(a_n + jy)}{z^2 - (a_n + jy)^2} dy. \end{aligned}$$

Let us chose $a_n = n$ and $b_n = n\pi + \pi/2$, we then have (recall that $\zeta \in [0, 1)$)

$$|g_\zeta(x - jb_n)|^2 = \frac{|\cosh(\zeta x + j\zeta(n + 1/2)\pi)|^2}{|\sinh(x + j(n + 1/2)\pi)|^2} = \frac{\sinh^2(\zeta x) + \cos^2(\zeta(n + 1/2)\pi)}{\cosh^2 x} \leq 2$$

and

$$|g_\zeta(a_n + jy)|^2 = \frac{|\cosh(\zeta n + j\zeta y)|^2}{|\sinh(n + jy)|^2} = \frac{\sinh^2(\zeta n) + \cos^2(\zeta y)}{\sinh^2 n + \sin^2 y} \leq \frac{\sinh^2(\zeta n) + 1}{\sinh^2 n} \leq 2.$$

We thus have,

$$\begin{aligned} \left| \oint_{\partial D_n} \frac{g_\zeta(s)}{z-s} ds \right| &= |X_n + jY_n| \\ &\leq 2\sqrt{2}|z| \left(\int_{-a_n}^{a_n} \frac{1}{|z^2 - (x - jb_n)^2|} dx + \int_{-b_n}^{b_n} \frac{1}{|z^2 - (a_n + jy)^2|} dy \right) \\ &\leq 2\sqrt{2}|z| \left(\int_{-\infty}^{+\infty} \frac{1}{|z^2 - (x - jb_n)^2|} dx + \int_{-\infty}^{+\infty} \frac{1}{|z^2 - (a_n + jy)^2|} dy \right). \end{aligned}$$

We easily conclude by the dominated convergence Theorem that, $\lim_{n \rightarrow \infty} \oint_{\partial D_n} \frac{g_\zeta(s)}{z-s} ds = 0$. This ensures the relation (19).

Let us now prove the equality (20).

Let us first observe that $\frac{\partial f_\zeta(z)}{\partial \xi} = sg_\zeta(z)$ for every $z \in \mathbb{C} \setminus j\pi\mathbb{Z}$. Observe also that $f_0(z) = 0$. By the dominated convergence theorem, we can integrate term by term the sum appearing in (19) to obtain

$$\begin{aligned} f_\zeta(z) &= \zeta + 2s^2 \sum_{k=1}^{\infty} \frac{(-1)^k}{z^2 + (k\pi)^2} \int_0^\zeta \cos(k\pi x) \, dx \\ &= \zeta + 2s^2 \sum_{k=1}^{\infty} \frac{(-1)^k}{z^2 + (k\pi)^2} \frac{\sin(k\pi\zeta)}{k\pi} \\ &= \zeta + 2 \sum_{k=1}^{\infty} \left(\frac{1}{(k\pi)^2} - \frac{1}{z^2 + (k\pi)^2} \right) (-1)^k k\pi \sin(k\pi\zeta). \end{aligned}$$

Finally, by developing in Fourier series the 2-periodic function defined by $\zeta \mapsto \zeta$ on $(-1, 1)$, we obtain

$$\zeta = -2 \sum_{k=1}^{\infty} \frac{(-1)^k \sin(k\pi\zeta)}{k\pi} \quad (\zeta \in [0, 1)).$$

This concludes the proof. □